

Airborne Ultra-Wideband Radars for Polar Research

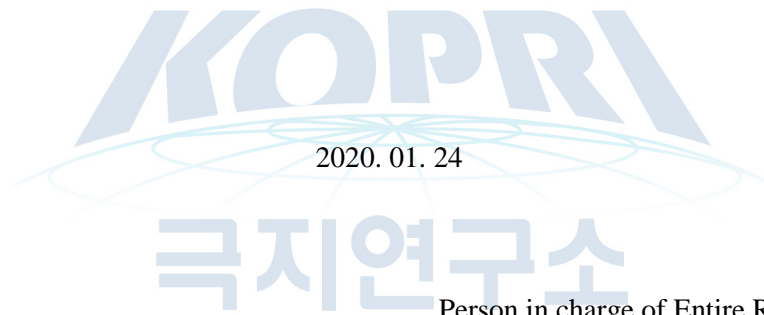
2020. 1. 24

REMOTE SENSING CENTER
THE UNIVERSITY OF ALABAMA

Submission

To : Chief of Korea Polar Research Institute

This report is submitted as the final report of entrusted research “Airborne Ultra-Wideband Radars for Polar Research” project of “Antarctic subglacial topography (BEDMAP) survey using unmanned system” project.



Person in charge of Entire Research: Joohan Lee

Name of Entrusted Organization: Remote Sensing Center, The University of Alabama

Entrusted Researcher in charge: S. Gogineni

Participating Entrusted Researchers: C. O'Neill

“ : Yang-Ki Hong

“ : J. B. Yan

“ : R. Taylor

Summary

I. Title

Annual Progress Report - Airborne Ultra-Wideband Radars for Polar Research

Researchers: S. Gogineni, C. O'Neill, Yang-Ki Hong, J. B. Yan and R. Taylor

Students: L. Li, J. Nunn, S. Kolpuke, H. Won, B. Bryant, A. Horstman and J. Glidden

II. Purpose

The primary objective of the project is to design and develop an ultra-wideband (UWB) radar that operates over its full frequency range of 170-470 MHz or any selected sub-band in this frequency range. The ability to select the center frequency and bandwidth will allow the selection of optimum radar parameters for sounding and imaging different areas in Antarctica.

III. R&D Efforts

We are designing the radar for sounding ice as thick as 5 km in Antarctica and imaging a maximum swath of about 3 km on either side of the aircraft flight path [Rodriguez-Morales, et al, 2014 and Stumpf, 2015]. The realized swath depends on the ice thickness and aircraft altitude over the ice surface. We are designing the UWB radar with the largest possible antenna array mounted under the wings to enable following requirements:

- 1) Measure ice thickness for generating 3-D topography of the ice-bed for selected areas and 2-D reflectivity maps of the ice-bed to determine basal conditions;
- 2) Map near-surface internal layers with fine resolution of about 50 cm and also deep internal layers with resolution of about 100 cm to determine long-term accumulation rates and understand flow dynamics; and
- 3) Collect data to estimate surface- and bottom-melt rates of ice shelves using wide-swath imaging and fine-resolution capabilities of the ultra-wideband radar.

IV. R&D Results

Over the last year, we made significant progress in designing and testing a prototype ultra-wideband radar by leveraging off the ongoing research at UA to develop UWB radars for remote sensing of snow, ice and soil moisture. In this report, we provide our progress over the first year of the project. We completed the following tasks:

- 1) Completed a system-level design of the ultra-wideband radar for sounding and imaging of ice;
- 2) Developed and tested sub-systems required to build the radar;
- 3) Designed an antenna array that can be installed under the wings of small lightweight aircraft;
- 4) Prototyped an antenna element and evaluated its performance;
- 5) Designed the digital sub-system; and
- 6) Developed algorithms to process data to be collected with the UWB radar.

Table of Contents

Chapter 1	Introduction
Chapter 2	Current R&D Status
Chapter 3	R&D Efforts
Chapter 4	R&D Results
Chapter 5	Conclusions
Chapter 6	References
Appendix	



Chapter 1 Introduction

The University of Alabama (UA) Remote Sensing Center received funding from the Korea Polar Research Institute (KOPRI) for the development of an ultra-wideband (UWB) radar with the largest possible antenna-array for airborne sounding and imaging of ice sheets. We designed the UWB radar to be operable with either its full bandwidth (170-470 MHz) or any selected sub-band. This feature will allow for the selection of optimum radar frequencies suitable for different areas in Antarctica. We designed the radar for sounding the thickest ice in Antarctica (~4.7 km) and imaging a swath width up to 3 km on either side of the aircraft flight path. The swath will depend on the ice thickness and aircraft altitude over the ice surface. Equipped with the largest possible antenna array, the UWB depth sounder/imager radar designed by UA and can be mounted on any short-range aircraft. It offers capabilities to:

- (1) Measure ice thickness for generating 3-D topography of the ice-bed for selected areas and 2-D reflectivity maps of the ice-bed to determine basal conditions;
- (2) Map near-surface internal layers with fine resolution of about 50 cm and also deep internal layers with resolution of 1-2 m to determine long-term accumulation rates and to understand flow dynamics; and
- (3) Collect data to estimate surface- and bottom-melt rates of ice shelves using wide-swath imaging and fine resolution capabilities of the ultra-wideband radar.

Chapter 2 Current R&D Status

2.1 Background

Fretwell et al. [2013] compiled airborne radar measurements carried out by various institutions around the world over the last 40 years and generated a new bed map for Antarctica. Nonetheless, many parts of the continent still remain unmapped. In some cases, only one thickness measurement exists over distances as large as 100-200 km. This contributed to highly inaccurate representation of the bed topography in BEDMAP2 due to poor spatial sampling –the error is particularly large in high relief regions.

Paving the way for next-generation computational ice-sheet models requires fine-resolution bed topography — particularly over areas undergoing rapid changes. Also, accurate information on the short-term and long-term accumulation rates are needed. While the depth-sounder data collected as part of NASA’s Operation Ice Bridge (OIB) mission over the past seven years have been extremely valuable [Fretwell et al., 2013, Thomas et al., 2011], even more scientifically sought-after data are within the reach of UWB radars operated from manned and unmanned aircraft.

UWB radars have been developed and successfully used over the last few years [Gogineni et al., 2015; Wang et al., 2016; Yan et al., 2017]. In this project, we made significant progress in designing and testing a prototype ultra-wideband radar by leveraging off the ongoing research to develop UWB radars for remote sensing of snow, ice and soil moisture. Although design and development of an UWB microwave radar is not a part of project funded KOPRI, we have agreed to provide a microwave radar available at UA for inclusion in the airborne instrumentation package to collect data needed to mass balance and other scientific research.

Chapter 3 R&D Efforts

3.1 Research during 2019

The major research tasks to be addressed during the first year of the project are the following:

- 1) Design, simulate, build and test the ultra-wideband (UWB) radar sub-systems including the transmitter, receiver and antenna array;
- 2) Design and simulate digital sub-systems including the chirp generator and digitization sub-sections;
- 3) Design and simulate antenna array, and build a prototype antenna to test and evaluate its performance;
- 4) Integrate all sub-systems into a single-channel radar prototype for extensive evaluation in the laboratory; and
- 5) Simulate the impact of antenna arrays and associated structure on aircraft performance.

We have significant progress on all the tasks listed above. We provide a summary of the progress made over the last 12 months.

3.2 Science requirements and system specifications

The large ice sheets in Greenland and Antarctica have a large potential to modulate sea level rise over the next century. They contain enough fresh water to raise sea level by more than 65 meters if they were to melt completely. Recent satellite and airborne observations show increased discharge and contribution from both ice sheets to sea level rise [Bamber et al., 2019; Rignot et al., 2019; Hanna et al., 2013; Shepherd et al., 2012; Pritchard and Vaughn, 2007, Rignot et al., 2011]. The social and economic impacts of rising sea level depend on our ability to adapt to and mitigate against its consequences. This in-turn depends on our ability to accurately project the rate of expected sea level rise. The Intergovernmental Panel on Climate Change (IPCC) projects that the sea level would increase between 26 and 96 cm over the century under different climate scenarios. However, more recent empirical studies show that this could be as large as 2 m [Bamber et al., 2019].

Table 1. Science requirements and mapping to objectives stated in the introduction.

<i>Measurement</i>	Objective	Required Accuracy	Spatial Sampling	Radar
<i>Ice thickness</i>	Objective #1	1 m (range)	1000 m 10-100 m for margins and outlet glaciers	UWB depth sounder/imager
<i>Reflectivity at the bed (basal conditions)</i>	Objective #1	0.5 dB	100 m pixel	UWB depth sounder/imager
<i>Water layer thickness (frozen or bed bed)</i>	Objective #1	0.5-4 mm	100 m survey 10 m hi-res	UWB depth sounder/Imager
<i>Internal layer depth and geometry</i>	Objective #2	3-10 cm for shallow layer 60-100 cm for deeper	100 m survey 10 m hi-res	UWB Microwave radar for shallow layers UWB depth sounder/imager for deeper layers
<i>Bottom melt rates</i>	Objective #3	50 cm or better	100 m coarse 10 m fine res	UWB depth sounder/imager

NASA has recently launched Ice, Cloud, and Land Elevation Satellite-2 (ICESat-2) for monitoring polar regions and is also planning to launch NASA-ISRO Synthetic Aperture Radar (NISAR) during 2021-2022. ICESat-2 is measuring changes in surface elevations of large ice sheets in Antarctica and Greenland for determining their current mass balance. It is also being used for freeboard measurements over sea ice to estimate its thickness [Abdalati, et al., 2010]. ICESat-2 supplements and complements CryoSat-II radar altimeter surface-elevation and free-board measurements [Wingham, et al., 2006]. A major objective of the NISAR mission is to measure surface velocities of both large ice sheets. The changes in surface elevations would provide information necessary to document mass loss or gain, and surface velocities would provide information on the speed-up and slow-down of outlet glaciers [Howat, et al., 2007]. However, additional information on ice-bed topography and basal conditions is essential to develop diagnostic and prognostic ice-sheet models [Fretwell et al., 2013]. In addition, the spatial variance of snow accumulation is needed to interpret satellite altimeter measurements of surface elevation and determine the mass balance of ice sheets using the flux approach. No satellite sensors to perform ice thickness and snow accumulation are currently available. Airborne measurements are the only way to obtain ice thickness and snow accumulation over large areas.

Table 1 (previous page) provides the vertical and spatial resolution requirements for airborne measurements. Using this information, we determined radar system parameters listed in Table 2 both for the UWB depth sounder and imager and the UWB microwave radar. However, this phase of the project does not involve development of a microwave radar. We are planning to provide a microwave radar available at UA to perform necessary measurements in conjunction with depth sounder/imager.

Table 2. Specifications of the UWB radars.

	UWB Radar sounder/imager	Comment	Ultra-wideband Microwave Radar	Comment
Frequency range	170-470 MHz	Bandwidth selectable	2-18 GHz	
Transmit power	500-1000 W	Determined by power available from the aircraft	200 mW	
Mode of operation	Chirped pulse		FM-CW	
Antenna	8 Element cross-track array under both wings		Planar array under the fuselage	
Gain	10-14 dBi		10-20 dBi	
Pulse widths or chirp length	1 us and 10-20 us	1 us for shallow ice and 10-20 us for ice thicker than 1 km	20-100 us	
Pulse repetition frequency	10 kHz		4 kHz	
Waveform Generation	8 channel 16-bit DDS		2 channel UWB chirp generator	
Digitization	14 bits		12 bits	
Sampling rate	1.2 - 2.5 GHz		500 MHz	

Chapter 4 R&D Results

4.1 UWB radar

We proposed to address the following major tasks to develop the UWB depth sounder/imager during the 1st year of the project:

- 1) Design, simulate, build and test the ultra-wideband (UWB) radar sub-systems including the transmitter, receiver and antenna array;
- 2) Design and simulate digital sub-systems including the chirp generator and digitization sub-sections; and
- 3) Integrate all sub-systems into a single-channel radar prototype for extensive evaluation in the laboratory.

We completed all three major tasks mentioned above during the 1st year as discussed below. We have completed the system-level design of the UWB radar depth sounder/imager operating over the frequency range of 170-470 MHz. Table 1 shows the link budget analysis of the radar for sounding 5 km thick ice. The signal-to-noise ratio, $\frac{S}{N}$, for a radar sounder operating over a smooth surface is given by

$$\frac{S}{N} = \frac{P_T G_T G_r \lambda^2 |\Gamma_{ib}|^2 (1 - |\Gamma_{is}|^2)^2 C_I C_P}{[8\pi(h + d\sqrt{\epsilon_r})^2 K T B F Loss]} \quad (1)$$

where P_T = Peak transmit power, 1 kW, G_T = transmit antenna gain, G_r = receive antenna gain, λ = wavelength in meters, Γ_{ib} = reflection coefficient at the ice-bed

interface, Γ_{is} = reflection coefficient at the air-snow interface; C_I = coherent integration gain, C_P = pulse compression gain, h = aircraft height above the ice surface in meters, d = ice thickness in meters, K = Boltzmann's constant, T = radar system temperature in Kelvins, B = radar receiver bandwidth in Hz (300 MHz), F = receiver noise figure and $Loss$ = two-way attenuation loss.

$$C_P = k \frac{T_u}{T_c} \quad (2)$$

Where T_u is uncompressed pulse width, T_c = compressed pulse width, and $k = 0.5$, a factor that accounts for mismatch filter loss used to reduce range sidelobes. $T_c = 3.3$ ns and $T_u = 10$ us.

C_I = coherent integration gain and it is given by

$$C_I = \sqrt{\frac{(h+d\sqrt{\epsilon_r})\lambda_g}{2} \frac{f_p}{v}} \quad (3)$$

where λ_g = wavelength in ice and f_p = pulse repetition frequency (PRF) in Hz, (9000 Hz), and v = aircraft velocity in m/s.

Let us assume that aircraft velocity is 50 m/s with radar operating in two modes: a short pulse (1 us) mode to sound shallow ice of 1 km or less and map internal layers and long pulse (10 us) mode to sound ice thicker than 1 km and map deeper internal layers. We will use the short pulse only once every 10 pulses to obtain higher sensitivity required for sounder thicker ice.

Table 3. S/N ratio obtained for 5 km thick ice and 20 dB/km two-way attenuation loss.

Parameter		320 MHz
1	Transmit Power, PT	60.0 dBm
2	Antenna Gain, GT*GR	24.0 dB
3	Wavelength, λ^2	-0.6 dBmeter ²
4	Two power transmission coefficient $(1- \Gamma ^2)^2$	-0.7 dB
5	Loss for 5 km thick ice (20 dB/km at 320 MHz)	-100.0 dB
6	Pulse compression gain, CP	31.8 dB
7	Integration gain, CI	40.6 dB
8	Spreading loss term-1, $(8\pi)^2$	28.0 dB
9	spreading loss term-2	78.6 dBmeter ²
10	Noise power	-85.2 dBm
11	Return loss for ice-bed interface	20.0 dB
11	Signal-to-Noise Ratio	13.7 dB

The S/N ratio for 5-km thick ice is about 13 dB, which is more than sufficient to determine thickness with the required accuracy and precision. There is also a large safety margin built into the design because of the higher 20 dB/km attenuation loss used in our design instead of typical 15 dB/km for interior cold ice reported in the literature [Matsuoka, et al.; 2010a and 2010b].

Figure 1 shows the block diagram of the radar being developed. The radar consists of three basic sub-systems excluding the antenna arrays: (1) digital sub-system; (2) RF transmitters; and (3) RF

receivers. The digital sub-system consists of command and control, a multi-channel arbitrary waveform generator (AWG), a multi-channel digitizer and a server to store digitized data and process and display data. Section 4.2 provides our plans to develop a compact digital sub-system. The UWB radar transmitter consists of 8 separate transmitters and 8 receivers, one for each element of the 8-element transmit array. Each transmitter consists of a bandpass filter, 2 driver amplifiers, 2 variable attenuators, 3 low-pass filters, a power amplifier, and a transmit/receiver (T/R) switch. The output signal from AWG is passed through the bandpass filter to reduce out of band spurious signals and supplied to the first driver amplifier that amplifies it to a level required by the 2nd driver

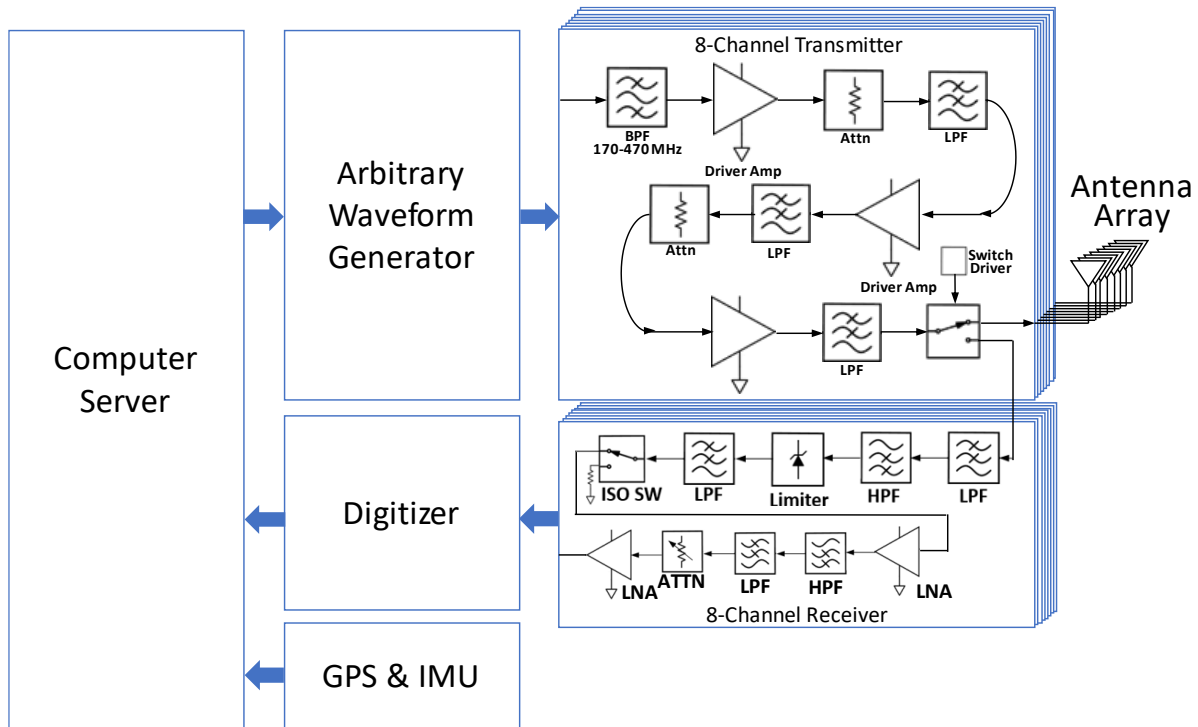


Figure 1. Block diagram of the UWB radar depth sounder/imager.

amplifier. The 1st driver amplifier output is passed through the first variable attenuator and the low-pass filter before it is supplied to the 2nd driver amplifier. The variable attenuators are to adjust the amplitude of the chirp signal and the low-pass filter is to reduce any harmonics above 470 MHz generated by the amplifier. We will transmit a low-power signal to sound and image shallow ice and a high-power signal to sound and image more glossy thicker ice. The attenuators are to reduce the transmit signal level for shallow ice sounding. The 2nd stage driver amplifier signal amplifies the signal to a level required to obtain 100-200 W peak power from the power amplifier. The amplified signal is passed through another attenuator and low-pass filter before it is supplied to the power amplifier. The power-amplifier output is coupled to one of the transmit-array elements through another low-pass filter, which again reduces any harmonics above 470 MHz generated by the power amplifier and the T/R switch. The switch protects the receiver from damage by the high-power transmit signals.

The receiver sub-system has 8 receivers, one for each element of the 8-element antenna-array. Each receiver consists of a bandpass filter, a limiter, a low-pass filter, a low-noise amplifier (LNA), a bandpass filter, two variable attenuators and a driver amplifier. Both bandpass filters are constructed using a low-pass and a high-filter. These bandpass filters reduce out-of-band spurious signals. We implemented the bandpass filter using low-pass and high-pass filters, so the receiver can be easily modified to operate at other frequencies up to 1 GHz. The limiter is to prevent receiver damage from any leakage signals during transmission. We selected the LNA, driver amplifier and attenuators to provide 20-60 dB amplification. We used the attenuators to reduce receiver gain to prevent its saturation from strong signals from shallow ice and increased gain to amplify weak signals from very thick ice to the level required for digitization. Figure 2 shows a prototype receiver board and its measured response. We have also completed the design and tests of high-power Transmit/Receiver (T/R) switches required for the radar. The measured maximum insertion loss at 500 MHz from the transmitter to antenna is about 1.4 dB and minimum isolation between the transmitter and receiver is about 49 dB during transmission.

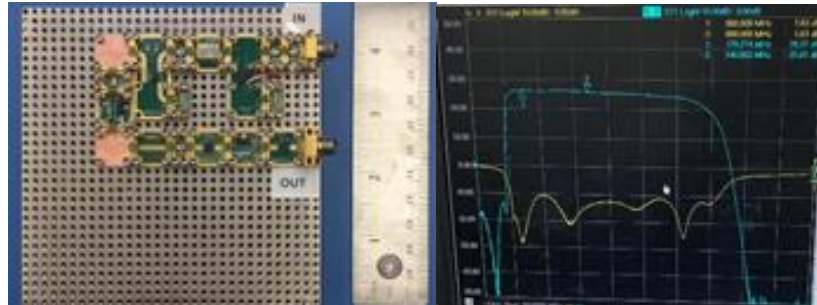


Figure 2: Receiver prototype and its measured response

Figure 2 shows a prototype receiver board and its measured response. We have also completed the design and tests of high-power Transmit/Receiver (T/R) switches required for the radar. The measured maximum insertion loss at 500 MHz from the transmitter to antenna is about 1.4 dB and minimum isolation between the transmitter and receiver is about 49 dB during transmission.

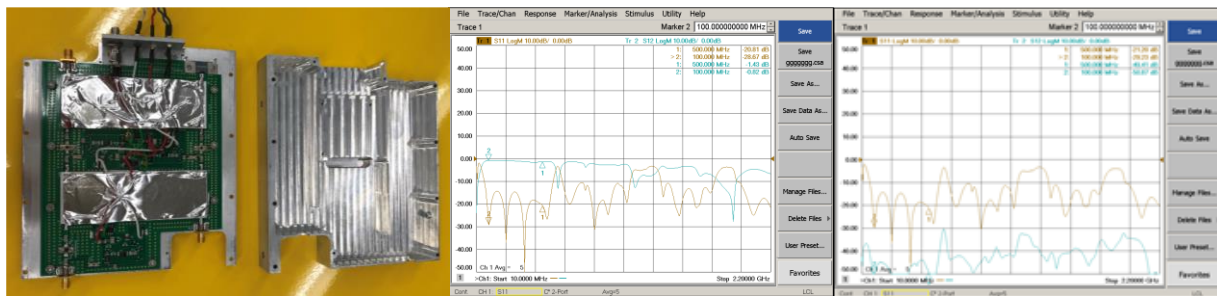


Figure 3: Prototype T/R module and its cover plate. The middle figure shows its measured insertion loss between the transmitter and antenna. The right figure shows the measured isolation between the transmitter and receiver.

We have already tested the prototype transmitter and receiver sub-systems as a part of the ongoing research in Greenland during August 2019. Figures 4a and 4b show the measured radar response using an optical delay line to a target at a range of about 3.75 km. Figure 3a shows measured time-domain signal and associated frequency spectrum. Figure 3b shows impulse response of the radar after pulse compression. The measurement shows that the loop-sensitivity of the radar is more than 210 dB. For these laboratory tests and measurements, we restricted the radar bandwidth to about 160 MHz instead of using full 300-MHz. We did this to prevent 2nd harmonic distortion caused by the power amplifier. For these tests we used commercial-off-the-shelf (COTS) amplifiers. We will be developing high power amplifiers with low harmonic distortion and peak power of about 200 W during the 2nd year of the project.

4.2 Digital sub-system

Two critical sub-sections of the 8-channel UWB radar

sounder/imager are the arbitrary waveform generator (AWG) and the data acquisition unit (DAQ). These systems must have low SWaP compared to current ones because of power and space constraints of the aircraft. The waveform generator must be capable of generating 8 chirps of 300-MHz bandwidth with pulse lengths between 1 and 10 μ s at a pulse repetition frequency of 9 kHz. Additionally, the DAQ must be able to digitize data at a rate of at least 600 MSPS.

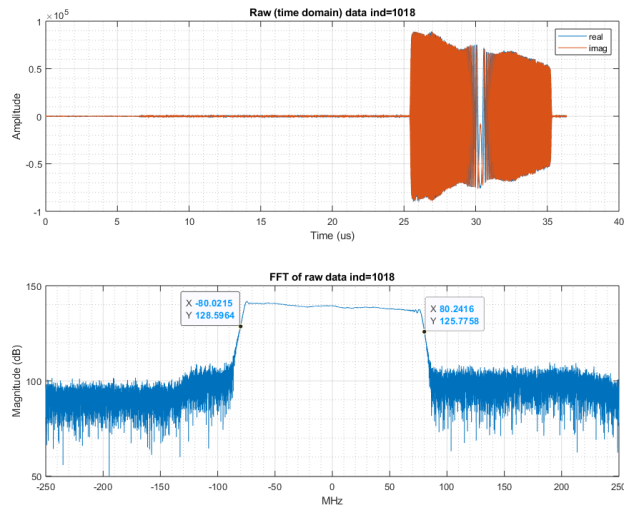


Figure 4a. Measured UWB radar wave form in time and frequency domains.

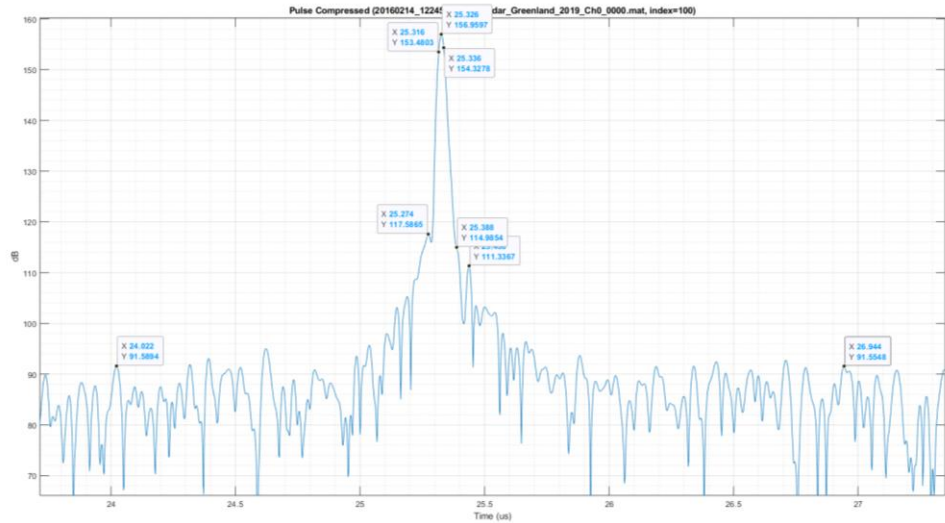


Figure 4b. Measured radar impulse response using an optical delay line to simulate a target at a range of about 3750 m. The far-off sidelobes are about 60 dB below the main peak.

A digital transceiver module is currently under development that will make use of new Xilinx Zynq Ultrascale+ RFSoc technology, specifically the ZXC49DR chip. It includes a 14-bit 16-channel transceiver built into the FPGA interconnect fabric capable of generating a waveform at 10 GSPS and acquiring data at 2.5 GSPS. The interconnect also includes a quad-core ARM Cortex-A53 processor to serve as the application unit and a dual-core ARM Cortex-R5 processor to serve as the real-time processing unit. The specifications of this module are shown in Table 4 as compared to the digital sub-systems currently in use in radars developed by the UA remote sensing center.

Table 4. Specifications of the digital sub-system being developed.

Subsystem	Current transceiver module	Proposed design
Tx sample clock rate	2.4 GSPS	10 GSPS
Tx up to	1.2 GHz	5 GHz
Rx sample clock rate	1.2 GSPS	2.5 GSPS
Rx up to	0.6 GHz	1.25 GHz
Channels (Tx x Rx)	8 x 8	16 x 16
Physical enclosure	17" x 22" x 7" (4U)	8" x 4" x 1.25"

The UWB radar sounder/imager needs only 8 channels to meet the science specifications required, therefore, half of the channels in the FPGA fabric will be disabled and unused, further reducing the power dissipation of the unit during the first phase of the project. The additional 8 channels can be used to digitize ultra-wideband microwave radar data in the future.

Figure 5 shows an initial 3-D model of the transceiver module. Figure 6 shows the system architecture and data flow. This system is currently under development using an evaluation system acquired from Xilinx.

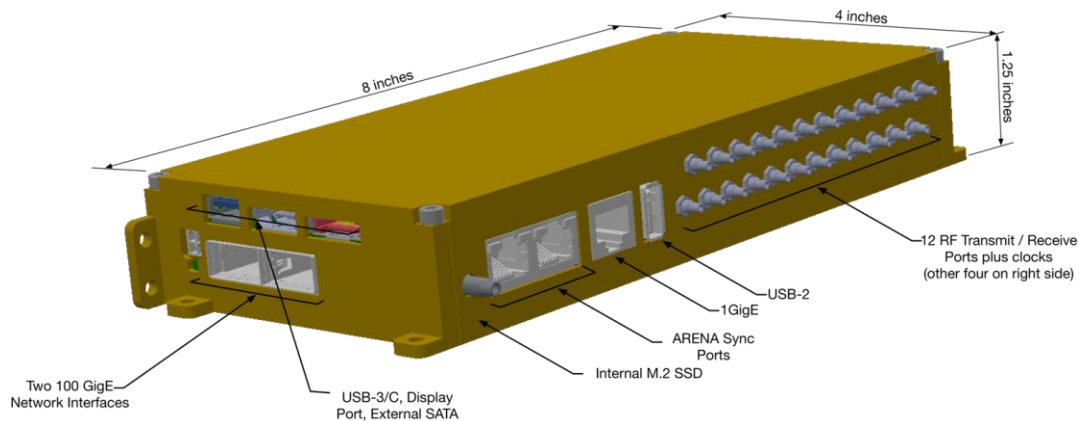


Figure 5. Digital sub-system that can serve both the radar sounder and UWB microwave radar.

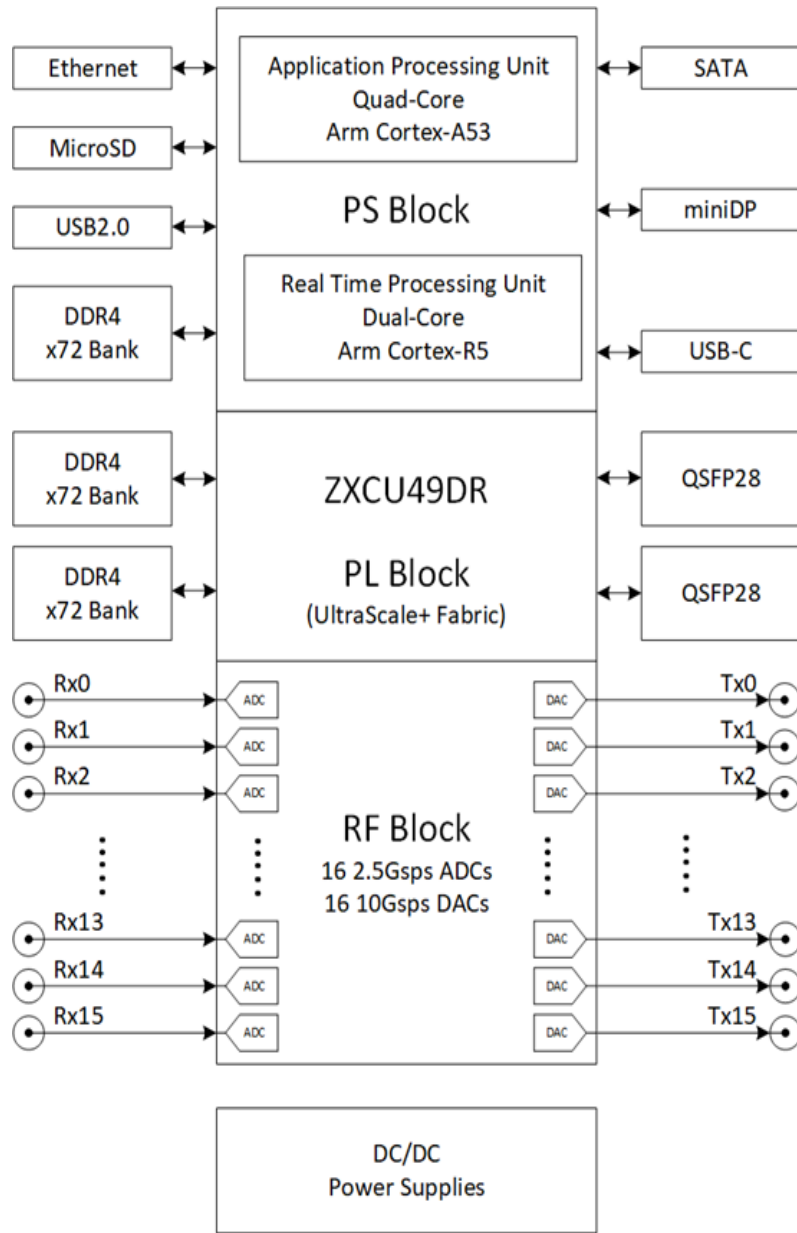


Figure 6. Digital sub-system block diagram.

We also have a digital transceiver system acquired as a part of other ongoing research at UA for testing purposes until the new digital sub-system development is completed. The existing digital sub-system consists of 8 transmit channels, operating at 2.4 GSPS, and 16 receive channels, operating at 1.2 GSPS.

4.3 Antennas and antenna arrays

The major tasks to develop antennas and antenna arrays this year are:

- 1) To design and simulate antenna array, and build a prototype antenna to test and evaluate its performance; and
- 2) To simulate the impact of antenna arrays and associated structure on aircraft communication performance.

4.3.A Sleeve dipole antenna

We have optimized the proposed sleeve dipoles to meet the bandwidth of 300 MHz and realized a gain of 10 dBi or higher as possible. Figure 7 shows the optimized sleeve dipoles with specifications and the simulated voltage standing wave ratio (VSWR) and realized gain over the frequency range of interest. The optimized sleeve-dipole shows a VSWR of 2:1, which is acceptable for radar operation, from 182 to 474 MHz (Bandwidth of 292 MHz) and realized gain of 6.81-12.0 dBi from 170 to 470 MHz. Compared to the reported sleeve dipole in the previous quarterly report, the optimized sleeve dipole exhibits 25 MHz higher bandwidth and 1.23-2.5 dBi higher realized gain.

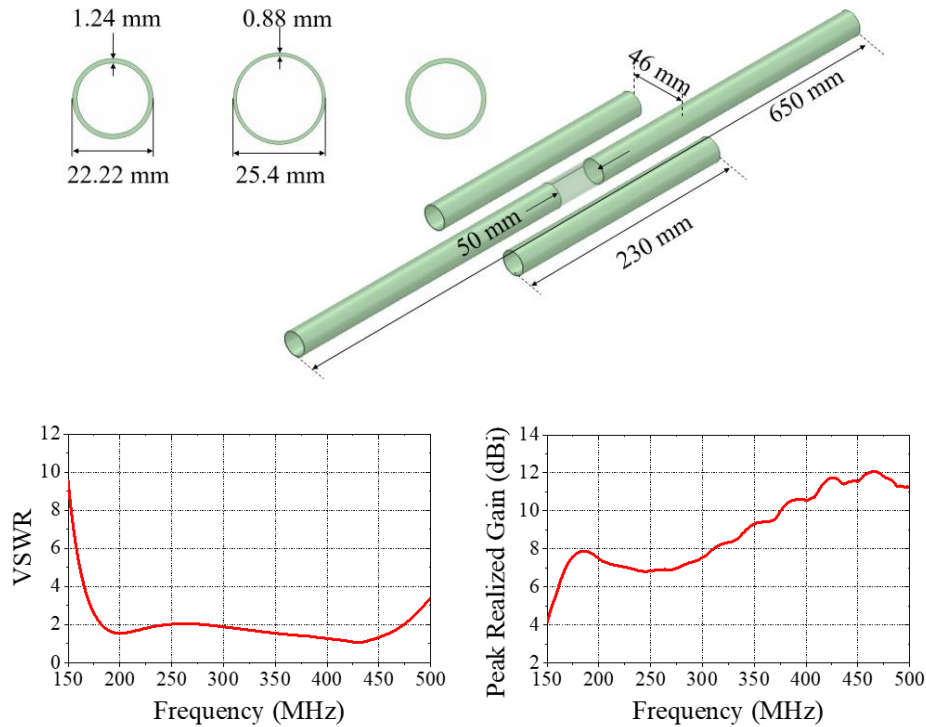


Figure 7. Antenna geometry and specification and simulated antenna performance over the frequency range of interest.

4.3.B. Sleeve dipole antenna with a fiberglass frame and Teflon tube

Fiberglass frames are used to cover the antenna to increase the mechanical strength, resist aerodynamic pressure, and allow RF cable and balun insertion. To rigidly hold the separated dipole, Teflon is used. Thus, the effects of the Polyurethane fiberglass frame (Dielectric constant: 1.08 and loss tangent: 0.0016 [Meyer, 2015]) and Teflon tube (Dielectric constant: 2.1 and loss tangent: 0.001 [Zemansky, 1982]) on the antenna performance are investigated. Figure 8 shows the optimized sleeve dipole with frame and its simulated VSWR and realized gain. As illustrated, the sleeve dipole with the fiberglass frame and Teflon tube slightly reduces the maximum operating frequency from 474 to 467 MHz and the realized gain of 0.4 dBi over the frequency of interest.

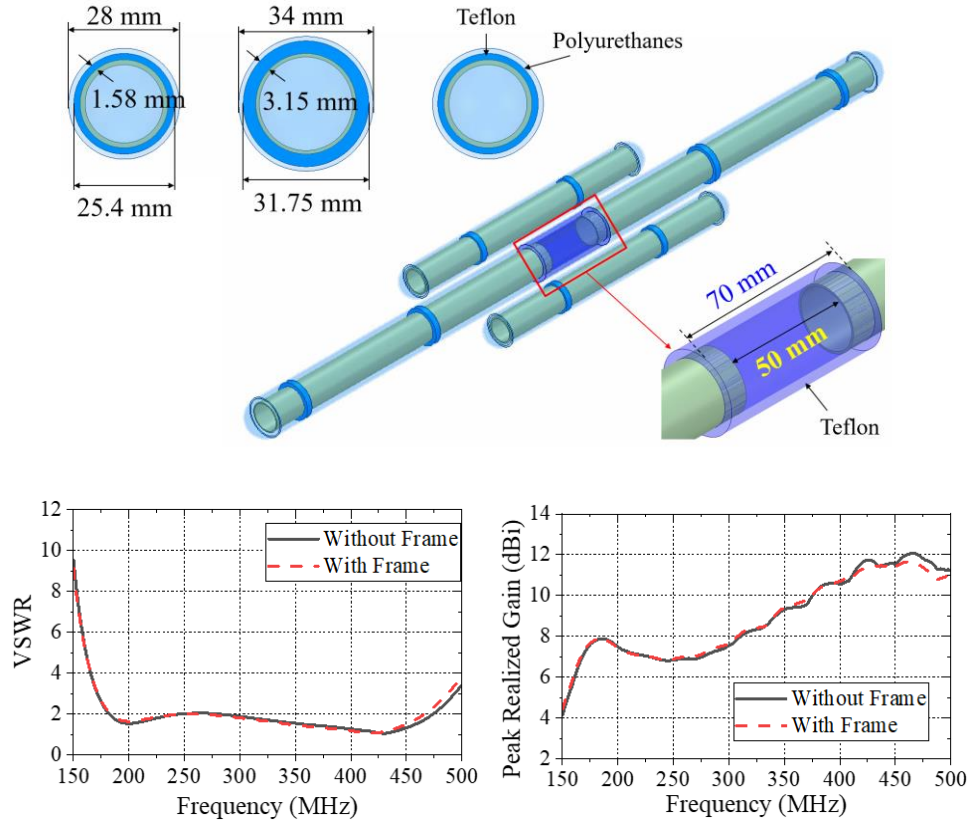


Figure 8. Antenna with casing geometry and specification and its simulated performance over the frequency range of interest.

4.3.C. Sleeve dipole antenna with a fiberglass frame and Teflon tube under carbon-composite CTLS wing model

A simplified perfect electric conductor (PEC)-based wing model (2600 mm wide, 5400 mm long, and 1 mm thick) is used for the above simulations. The realistic CTLS wing model with carbon fiber reinforced epoxy composites (CFRPs), having a resistivity of 2000 lower than the value of the aluminum [Leininger, 2012], was developed in the simulation to investigate the effects of the aircraft wing structure and material on the antenna performance. Figure 9 shows the configuration of the proposed sleeve antenna with the frame under the CFRP-based CTLS wing and its VSWR and realized gain performance. The proposed sleeve antenna under the CFRP-based CTLS wing shows the VSWR of 2:1 from 190 to 430 MHz and realized gain of 5-13 dBi.

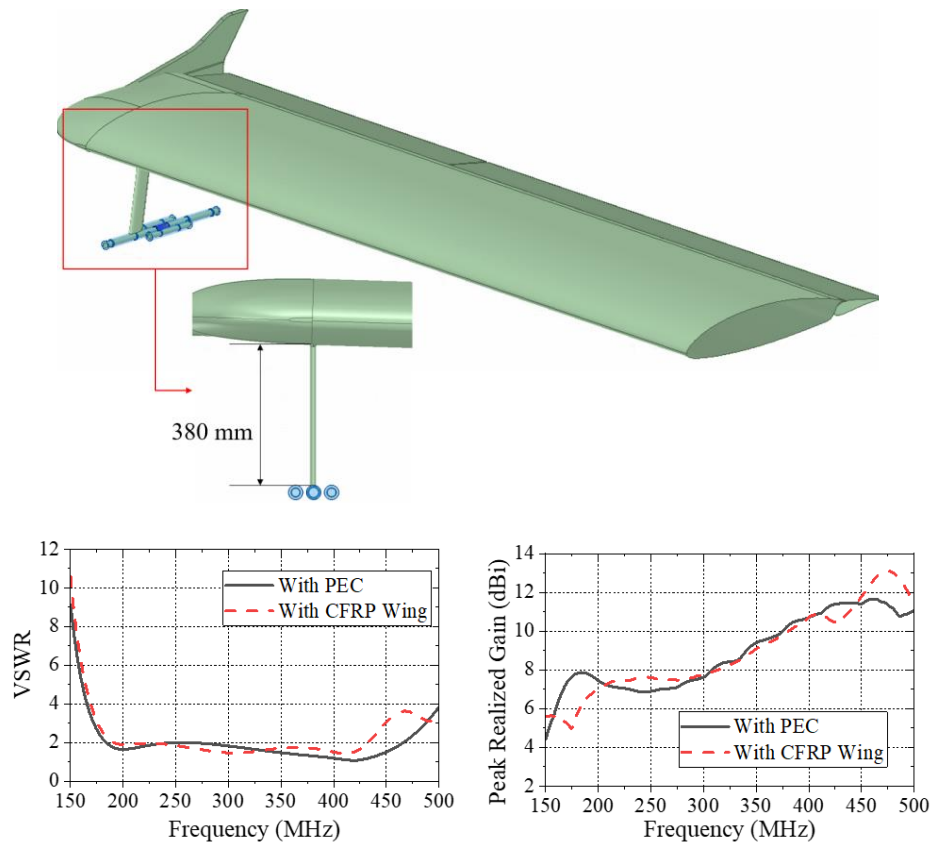


Figure 9. Antenna with frame under CTLS wing geometry and specification and simulated antenna performance.

4.3.D. Sleeve dipole antenna array with a fiberglass frame and Teflon tube under carbon-composite CTLS wing model

To enhance the minimum realized gain up to 10 dBi, we used two four-element sleeve dipole antenna-array, one located under each wing. Figure 9 shows the configuration of the proposed sleeve dipole antenna array on right CTLS wing, VSWR and overall realized gain. The element 1 and 3 show the VSWR of 2:1 from 190 to 430 MHz, while the element 2 and 4 show the VSWR of 2:1 from 190 to 450 MHz. The simulated bandwidth is degraded due to the wing structure. On the other hand, the overall realized gain is increased, compared to the single antenna element. The 4-element sleeve dipole antenna array can achieve 8.2-19.3 dBi of realized gain. The 8-element array will have gain that varies between 11-22 dBi.

We will further optimize antenna performance to extend the lower and upper frequency range to cover 170-470 MHz range with the design of the balun or matching networks.

4.4 Platforms & Integration

The Platforms & Integration focus area objectives in year 1 are to:

- 1) Define and polish scientific and instrumentation requirements;
- 2) Define system requirements for the UWB radar, RF, and digital sub-systems
- 3) Design and build a prototype antenna element

This report focuses on objective #3. Objectives 1 and 2 are in prior reports and sections.

The current expected aircraft platform is the Flight Design CTLS aircraft, a light sport aircraft with a 1320 lbf gross weight, a 28 ft. wing-span, and a water-cooled 100 hp Rotax 912 ULS engine. The aircraft load limits are +4/-2 g with a Vne of 145 KCAS. The CTLS structure is a monocoque fuselage with a cantilever wing and stabilizer. The primary aircraft structure is composed of carbon fiber, aramid, and foam composite sandwich construction. We are modifying the aircraft with an 8 element VHF antenna array, radar equipment, and associated systems. An autonomous flight control system (AFCS) for semi-to-fully autonomous operations is included in the design. Figure 10 shows the integrated aircraft and radar system.



Figure 10. Flight Design CTLS with VHF antennas, pylons, radar systems, and autonomous flight control system

4.4.A Antenna Design

The antenna elements are a sleeve-dipole configuration designed to operate in the 170–470 MHz VHF/UHF band. Each sleeved-dipole has a 670mm dipole with two 290mm parasitic elements spaced 62mm from the dipole. Figure 11 shows the pylon and pod configuration and dimensions. Each 15.5” pylon is designed to attach to the aircraft’s ribs spaced at 22 inches with the forward pylon connected to the wing spar structure. The volume forward of the spar contains full span fuel tanks and was not considered as feasible for structural attachment. Fiberglass frames and skins tie the antenna elements together and to the pylons. The RF cable is routed through the forward pylon.

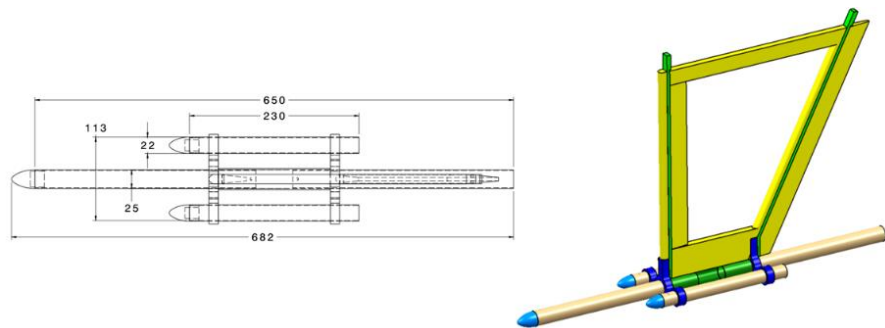


Figure 11: Antenna & Pylon Configuration

The structural loads were defined by applying inertial and aerodynamic flight loads to the pylon and antenna. Critical load cases are: 1) Inertial sideload forces during a roll, and 2) Sideslip maneuvers at 145kt Vne. Vertical acceleration load cases are not critical for this design. The critical structural component is the

wing-pylon interface with lateral bending moments (i.e. sload induced moments). We strongly stress that dedicated pylon hardpoints at the spar are necessary, which will require detailed engineering collaboration with the aircraft company.

4.4.B Structural Simulation

We simulated the structural load cases with ANSYS and iterated the design to optimize the structural weight, configuration, and interfaces. The individual antenna, sleeve, and bowtie connectors remain well within the maximum deflection and stress limits with a factor of safety exceeding 10x. We will investigate using even thinner wall tubing for the antenna elements. A future iteration of the bowtie connectors will remove the outer wall and reduce the thickness further. We did replace the original sleeve with the thinnest FR4 tubing that we can source.

The coupled antenna and pylon structural simulations indicated that the critical area is the aircraft to pylon interface. One critical load case is the aerodynamics sideslip at V_{ne} . The simulated pylon stress and deflections are shown in Figure 12. The roll rate case shows a similar behavior. We believe that the use of diagonal jury struts between the pylons, as discussed in the previous report, is warranted to reduce the pylon's spar weight and structural attachment complexity. We see a clear optimization curve for performance and configuration, especially for the aerodynamic side loads associated with fairings over pylon spars and the inertial loads associated with pylon and antenna mass.

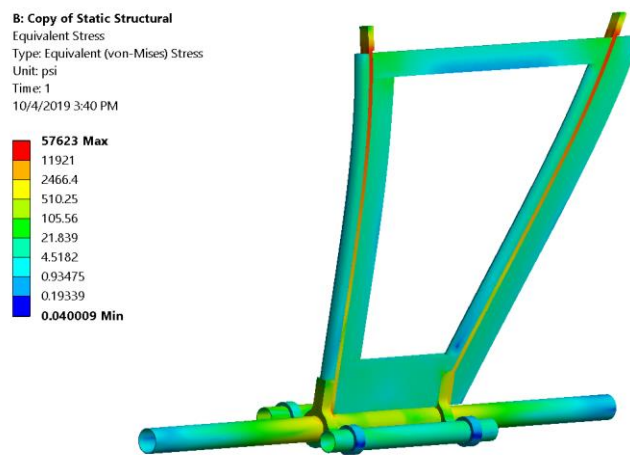


Figure 12. Aerodynamic sideslip stresses at V_{ne}

4.4.C. Prototype Antenna

We built a prototype of the antenna, balun, and pylon for RF, configuration, and structural evaluations. This prototype uses 1" and 7/8" aluminum tubing with 0.035 inch wall thicknesses. We used a 1 inch FR4 fiberglass reinforced composite pipe as the dipole connector sleeve, which provides both dipole structural bending stiffness and alignment. Screws connect the sleeve and tubes, which have flush-mounted nutplates installed into the inner wall. Ultra high molecular weight polyethylene bowties connect the dipole elements and parasitic elements and provides a structural attach point to the pylon. Nose-cones cap the forward element tubes. As this prototype is designed for functional testing of the antenna and pylon system, the RF feed is constructed of connectorized RF components despite the weight penalty. We plan a switch to an integrated coax cable, balun, and feed in a future iteration. Our prototype of the antenna, pylon, and connectorized balun shown in Figure 13 weighs 0.94 lbs (492g). This is below the target weight.

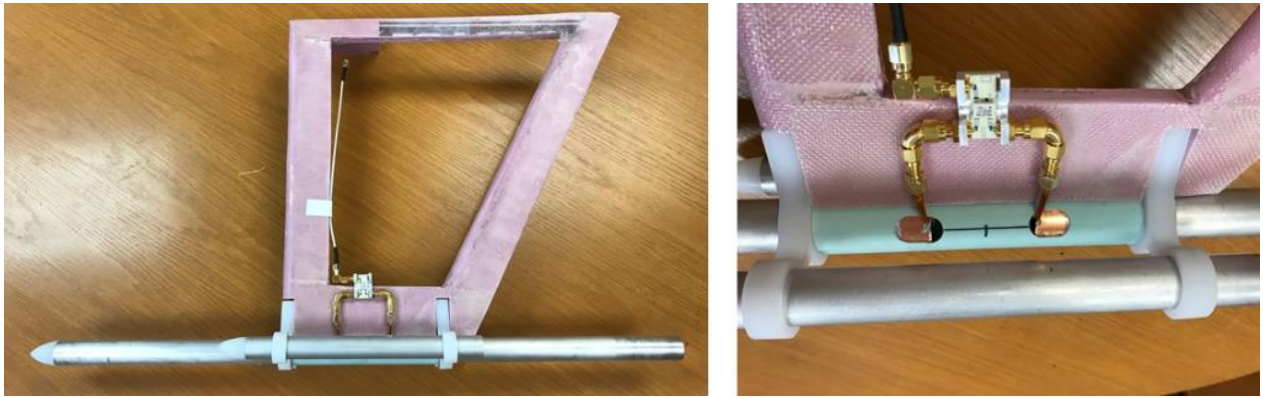


Figure 13. Prototype Antenna & Pylon

We tested the prototype antenna and pylon with a Fieldfox vector network analyzer to characterize the RF performance. The test was performed outdoors and with a metallic ground plane to simulate the aircraft's wing. The test was conducted between 100 to 500 MHz for a single element. Figure 14 is representative of the current design on the CTLS aircraft and provides an experimentally measured -10dB bandwidth of 200 to 430 MHz. The measured return loss about 20 dB or lower over the frequency range of 240 to 400 MHz. By changing balun impedance we can extend the frequency range in the lower and upper ends of the frequency range. We can also incorporate a matching network into the input of each antenna element and increase the frequency range from 170 to 470 MHz.

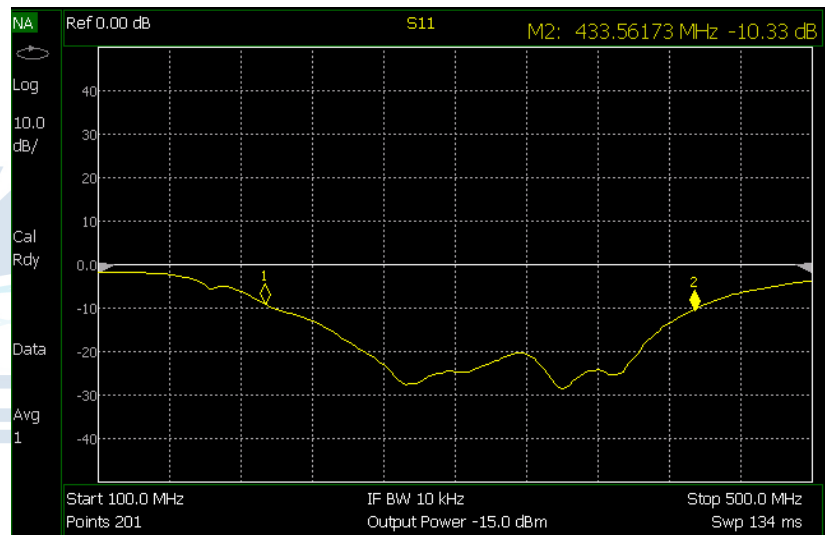


Figure 14. RF return loss performance of the prototype antenna and pylon

4.5 Aircraft & Systems Design

We updated the weight & balance of the full integrated radar and aircraft system to reflect the radar and digital system design choices and experimentally determined system weights. Table 5 indicates that the center of gravity (CG) of the fully integrated aircraft remains within the acceptable range of 11.1 inches to 18.8 inches aft of the leading edge. The W&B and gross weight remains feasible.

We identified design characteristics and action items that are necessary for further development and performance optimization:

- KOPRI and UA must coordinate with the aircraft company to provide structural attach points and access holes for the pylons and radar equipment.
- UA will consider further miniaturize of the radar systems
- KOPRI and UA must collaborate to create a power management strategy for normal and emergency operations.
- KOPRI and UA must collaborate and interact in the design, placement, and development of the autonomous flight control system and the radar system.

Table 5: Weight & Balance

		Weight [lb]	Arm [in]	Moment [lb-in]
CTLS Aircraft	Aircraft (dry)	700	13.3	9310
	Pilot (std)	170	3.9	662
	Fuel (35 gal)	212	8.3	1758
	Luggage (aft)	30	45.0	1350
AFC	Flight Control	80	-5.5	-440.0
Radar	Radar Equipment	90	21.8	1962
	Antennas (8x)	10	18.0	180
	Wing Connect (8x)	12	20.0	240
	Cables (8x)	14	28.4	417
Total Aircraft		1318		15438
		CG	11.7	in

Chapter 5 Conclusion

We have made significant progress in all aspects of the project over the last 12 months. We are well positioned to develop a compact and lightweight UWB radar for integration into a light aircraft as proposed during the 3rd year. We are preparing technical reports on the system design, sub-system designs and simulations, and antenna-array design and simulations. The technical reports will provide a more detailed information of the summaries given in this report [O'Neill et al., *EUSAR 2020*; Won et al., *Manuscript in Preparation*]. These technical reports have been approved and submitted for publication and are included in the Appendix below.

Chapter 6 References

- Abdalati, W. et al., 2010. The ICESat-2 Laser Altimetry Mission. *Proceedings of the IEEE*, 98(5), pp. 735-751.
- Bamber J.L., Michael Oppenheimer, Robert E. Kopp, Willy P. Aspinall, Roger M. Cooke, Ice sheet contributions to future sea-level rise from structured expert judgment, *Proceedings of the National Academy of Sciences* May 2019, 201817205; DOI: 10.1073/pnas.1817205116
- Fretwell, P. et al., 2013. Bedmap2: improved ice bed, surface and thickness datasets for Antarctica. *The Cryosphere*, 7(1), pp. 375-393.
- Gogineni, S., J. B. Yan, D. Gomez-Garcia, F. Rodriguez-Morales, C. Leuschen, Z. Wang, J. Paden, R. Hale, E. Arnold, and D. Braaten. 2015. "Ultra-Wideband Radars for Measurements over ICE and SNOW." In *International Geoscience and Remote Sensing Symposium (IGARSS)*. <https://doi.org/10.1109/IGARSS.2015.7326753>.
- Hanna, E. F. J. Navarro, F. Pattyn, C. M. Domingues, X. Fettweis, E. R. Ivins, R. J. Nicholls, C. Ritz, B. Smith, S. Tulaczyk, P. L. Whitehouse, and H.J. Zwally, 2013. Ice-sheet mass balance and climate change. *Nature*, 498, pp. 51-59.
- Howat, I., Joughin, I. & Scambos, T., 2007. *Rapid Changes in Ice Discharge from Greenland Outlet Glaciers*, s.l.: Science Express.
- Leininger, M., et al., Advanced Grounding Methods in the Presence of Carbon Fibre Reinforced Plastic Structures, *Proceeding 2012 ESA Workshop on Aerospace EMC*, May 2012.
- Matsuoka, K., MacGregor, J. A., and Pattyn, F.: Using englacial radar attenuation to better diagnose the subglacial environment: A review, *Proceedings of the 13th International Conference on Ground Penetrating Radar (GPR) 2010*, 21–25 June 2010, Lecce, Italy, 1–5, doi:10.1109/ICGPR.2010.5550161, 2010a.
- Matsuoka, K., Morse, D., and Raymond, C. F.: Estimating englacial radar attenuation using depth profiles of the returned power, central West Antarctica, *J. Geophys. Res.*, 115, 1–15, doi:10.1029/2009JF001496, 2010b
- Meyer, G., Polyurethane Foam: Dielectric materials for use in radomes and other applications, *General Plastics Manufacturing Company*, Nov. 2015.
- O'Neill, C., Gogineni, S.P., Yan, J.B., Taylor, D., Li, L. High-Performance Polar Airborne Ultra-Wideband Radar Imaging Capability with a Light Sport Aircraft, *EUSAR 2020*. (See Appendix below.)
- Pritchard HD and Vaughan DG (2007) *Widespread acceleration of tidewater glaciers on the Antarctic Peninsula*. *J Geophys Res* 112:F03S29.
- Rignot EJ, Velicogna I, van den Broeke MR, Monaghan AJ, Lenaerts JTM (2011) Acceleration of the contribution of the Greenland and Antarctic ice sheets to sea level rise. *Geophys Res Lett* 38:L05503.
- Rignot, EJ, Jérémie Mouginot, Bernd Scheuchl, Michiel van den Broeke, Melchior J. van Wesseem, Mathieu Morlighem, Four decades of Antarctic Ice Sheet mass balance from 1979–

2017, Proceedings of the National Academy of Sciences Jan 2019, 116 (4) 1095-1103; DOI: 10.1073/pnas.1812883116

Rodriguez-Morales, F. et al., 2014. Advanced multifrequency radar instrumentation for polar research. *IEEE Transactions on Geoscience and Remote Sensing*, 52(5), pp. 2824-2842.

Shepherd A, et al. (2012) *A reconciled estimate of ice-sheet mass balance. Science* 338:1183–1189.

Sears, F, et al., *University Physics*, 6th ed, Addison-Wesley, 1982.

Stumpf, T., 2015. *A Wideband Direction of Arrival Technique for Multibeam, Wide-Swath Imaging of Ice Sheet Basal Morphology*, s.l.: University of Kansas.

Thomas, R., E. Frederick, J. Li, W. Krabill, S. Manizade, J. Paden, J. Sonntag, R. Swift, and J. Yungel. 2011. “Accelerating Ice Loss from the Fastest Greenland and Antarctic Glaciers.” *Geophysical Research Letters*. <https://doi.org/10.1029/2011GL047304>.

Yan, Jie Bang, Daniel Gomez-Garcia Alvestegui, Jay W. McDaniel, Yan Li, Sivaprasad Gogineni, Fernando Rodriguez-Morales, John Brozena, and Carlton J. Leuschen. 2017. “Ultrawideband FMCW Radar for Airborne Measurements of Snow over Sea Ice and Land.” *IEEE Transactions on Geoscience and Remote Sensing*. <https://doi.org/10.1109/TGRS.2016.2616134>.

Wang, Zongbo, Sivaprasad Gogineni, Fernando Rodriguez-Morales, Jie Bang Yan, John Paden, Carlton Leuschen, Richard D. Hale, et al. 2016. “Multichannel Wideband Synthetic Aperture Radar for Ice Sheet Remote Sensing: Development and the First Deployment in Antarctica.” *IEEE Journal of Selected Topics in Applied Earth Observations and Remote Sensing*. <https://doi.org/10.1109/JSTARS.2015.2403611>.

Wingham, D.J., Francis, C.R., Baker, S., Bouzinac, C., Brockley, D., Cullen, R., de Chateau-Thierry, P., Laxon, S.W., Mallow, U., Mavrocordatos, C., Phalippou, L., Ratier, G., Rey, L., Rostan, F., Viau, P., Wallis, D.W., *CryoSat: a mission to determine the fluctuations in Earth's land and marine ice fields*, *Adv. Space Res.*, 37 (2006), pp. 841-871

Won, H., Hong, Y.K., Bryant, B., Li, L., Choi, M., O'Neill, C., Yan, J.B., Gogineni, S.P. Open-Sleeve Dipole Antenna for an Airborne VHF/UHF Snow Measuring Radar, *Manuscript in Preparation*. (See Appendix below.)

Appendix

High-Performance Polar Airborne Ultra-Wideband Radar Imaging Capability with a Light Sport Aircraft

Charles O'Neill^a, Prasad Gogineni^a, Jie-Bang Yan^a, Drew Taylor^a, Linfeng Li^a

^aRemote Sensing Center, The University of Alabama, 401 7th Avenue, Tuscaloosa, AL 35487, USA

Abstract

Polar regions are among the least known and most challenging areas of Earth in terms of their topography, water mass and transport, and accessibility. This paper shows a solution for advanced SAR capabilities on a unique light sport aircraft (LSA) platform suitable for widespread radar measurements of Polar regions. The LSA is integrated with an 8 channel 170-470 MHz ultra-wideband (UWB) radar capable of sounding Polar ice sheets and ice layers down to the bed. We designed, constructed, and tested the sub-systems, including a test of the RF electronics with a surface vehicle on the Greenland icesheet.

1 Introduction

The Polar regions are a critical part of the Earth's dynamics, yet remain among the least understood and mapped areas of Earth. For example, the most extensive maps of Antarctica using 40 years of data [1] has regions with no data for hundreds of km. Currently, the science needs for high resolution bed and ice-layer measurements are only effectively feasible with aerial surveys. Existing surveys are often based on large aerial platforms (e.g. [2]). This project takes the lighter approach using the rapidly evolving light sport aircraft (LSA) to provide versatile, lightweight, cost effective and potentially autonomous platforms with high performance and multichannel radars capable of sounding the entire ice sheet. This paper discusses the development and testing of an 8 channel 1600W aerial MIMO aerial system integrated on an LSA aircraft.

2 Radar System Design

2.1 Link Budget

We determined the feasibility of this aerial radar to sound the oldest ice in Antarctica with the link budget in Table I. The ice-bed boundaries are considered to be large planar reflectors. Existing data indicates that our estimate of one-way ice loss of 20 dB/km at 320 MHz is conservative. These link budget calculations indicate that an 8-channel radar system with a total transmit power of 1600 W and an UWB antenna array with 7-12 dBi gain provides a SNR of just under 30 dB.

2.2 RF Electronics

The airborne UWB radar system is designed as a chirped pulse radar with 5 major parts: 1) RF transmitter (TX), 2) RF receiver (RX), 3) digital system, 4) computer server and 5) an 8-element antenna array. The radar system block diagram is shown in Fig. 1. The digital system has 8 transceiver channels. Each transmitter channel has a 14-bit 2.0 GSPS digital-to-analog converter (DAC). Each receiver channel has a 14-bit 1.0 GSPS analog-to-digital converter (ADC), which can digitize the received signal

TABLE I
1 UWB RADAR LINK BUDGET

Frequency	320 MHz
Pulse length	10 us
Bandwidth	300 MHz
Transmit Power	62 dBm
Antenna Gain (2-way)	24 dB
Air-ice power trans. coeff. (2-way)	-0.7 dB
Total ice loss	100 dB
Ice-rock reflection coeff.	-20 dB
Pulse compression gain	34.8 dB
Integration gain (hardware)	40.6 dB
Spreading loss term 1	28 dB
Spreading loss term 2	79.1 dB
Noise figure	3.5 dB
Noise power	-86 dBm
Received signal power	-72 dBm
Post processing integration gain	10 dB
SNR	29 dB

with up to 600 MHz bandwidth. The digital system directly generates the 170-470 MHz chirped pulse signal with a 10 us pulse width and a 10% duty cycle.

The TX chassis consists of 8 TX modules, each module has a driver amplifier (DA), a power amplifier (PA), and a low pass filter (LPF). The DA increases the power level

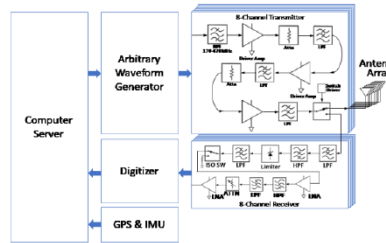


Fig 1. UWB Radar Block Diagram

required for the PA to obtain the 200 W output. The LPF is for suppressing the 2nd order harmonics generated by

the PA. A high-power switch after the filter selects the transmit or receive (T/R) mode of operation. Each 200 W RF output feeds one antenna element for a total power being fed to the 8-element antenna array of 1600 W. After the 10 us transmitting window, the T/R switch is set to receiving mode.

The RX chassis consists of 8 RX modules. Each RX module is cascaded by a high pass filter (HPF), a LPF, a high-power switch (HP SW), a limiter, an isolation switch (ISO SW), an LNA, a final pair of HPF and LPF filters and a final LNA. The filters remove spurious received signals. The limiter protects the receiver from being damaged by the high-power signal coupled from the transmitter. We selected the LNA is selected to have a low noise figure. The full receiver chain provides a 27 dB amplification.

2.3 Radar Simulation

The system design concept is evaluated and verified by a delay line simulation using Keysight Advanced Design System (ADS). Figure 2 shows the simulation block diagram for one RF transceiver module with 200W output power. Ideal amplifier models with gain and saturation settings are used for both the DA and PA in the transmit-

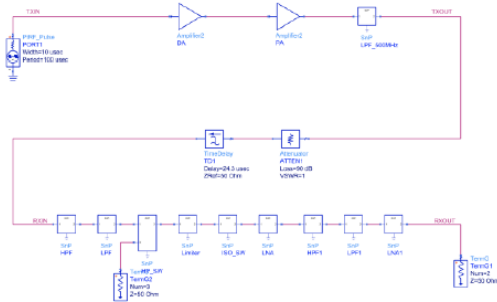


Fig 2. UWB Radar delay line simulation in ADS

ter. The other component models are real components with S-parameters either obtained by lab measurements or

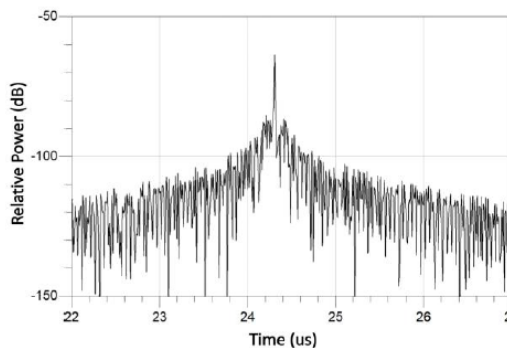


Fig 3. Simulated impulse response for ice bed returned signal

provided by manufacturers.

The ADS derived radar pulse compression impulse response is shown in Fig 3. The target is defined to simulate

the ice bed corresponding to a 24.3 us round-trip time equal to a free space distance of 7.29 km. We simulated the 2-way ice loss with a 90 dB attenuation. The radar loopback simulation shows a 250 dB sensitivity when including the hardware integration and 2-way antenna gain.

3 Platform Integration

The Flight Design CTLS aircraft is a LSA with a 600 kg gross weight, 8.6 m wing-span and a water-cooled 100 hp Rotax 912 ULS engine. The aircraft load limits are +4/-2 g with a Vne of 145 KCAS. The CTLS structure is a monocoque fuselage with a cantilever wing and stabilator. The primary aircraft structure is composed of carbon fiber and aramid fibers. Figure 4 shows the radar depth sounder antenna-array design concept. A four-element sleeve-dipole antenna-array can be mounted under each wing along the 0.56 m structural rib spacing of the wing panel.



Fig 4. Flight Design CTLS with VHF antennas, pylons, radar systems, and autonomous flight control system

We designed the configuration to allow virtual aperture along the cross-track direction for enhanced SAR operation. Each dipole element is integrated into a custom-designed fiberglass pod and is attached to the wing using a 0.4 m fiberglass pylon.

3.1 Antennas & Arrays

Antenna and array development required meeting the UWB requirements in a lightweight and low drag configuration.

3.1.1 Sleeve Dipole Antenna

We developed and optimized a sleeve dipole antenna to meet the bandwidth of 300 MHz and a gain of 10 dBi or higher. Figure 5 shows the optimized sleeve dipole con-

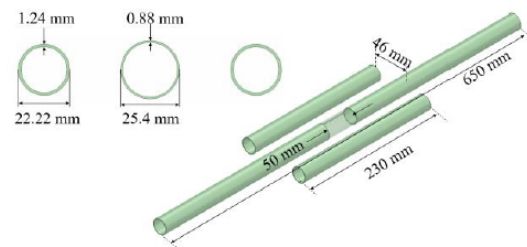


Fig 5. Sleeve Dipole Antenna Configuration

figuration and sizing. The optimized sleeve dipole shows

a VSWR of 2:1, which is acceptable for radar operation, from 182 to 474 MHz (Bandwidth of 292 MHz) and realized gain of 6.81-12.0 dBi from 170 to 470 MHz.

3.1.2 Integrated Array with a Composite Wing

The initial design used a simplified perfect electric conductor (PEC)-based wing model (2600 mm wide, 5400 mm long, and 1 mm thick); however, the actual CTLS wing uses carbon fiber reinforced epoxy composites (CFRPs). A CFRP model having a resistivity lower than the value of aluminum was developed in the simulation to investigate the effects of the aircraft wing structure and material on the antenna performance. Figure 9 shows the simulated VSWR and realized gain when integrated with the CFRP-based CTLS wing. The sleeve dipole antenna

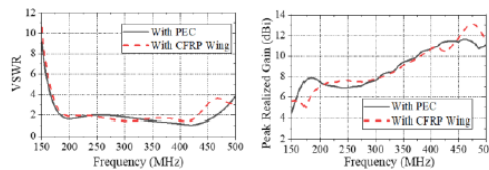


Fig 9. Antenna performance comparison between PEC and CFRP wing models

with the CFRP-based CTLS wing shows a VSWR of 2:1 from 190 to 430 MHz and a realized gain of 5-13 dBi.

3.2 RF Rack & Cables

The VHF equipment rack is approximately a 40 kg, 400 mm by 480 mm by 500 mm box containing the radar systems. While the CTLS has an aft baggage compartment, baggage door access constraints suggested mounting in the cabin area within the existing right-seat location. The existing CTLS cockpit is shown in Figure 10 showing the seats, flight control system (FCS), instrument panel, upper cabin structure, and the existing aft cabin structure. The equipment rack placement has multiple design constraints. A significant constraint is the cabin width at the seat: approximately 19 inches between the center tun-

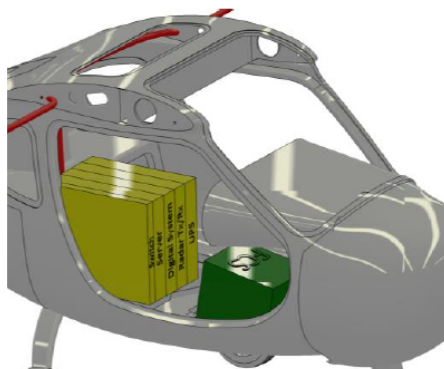


Fig 10. Cabin Configuration with installed radar equipment and flight control system

nel/console wall and the fuselage skin. An additional constraint is that the center tunnel/console contains the aircraft's propulsion FCS.

Each antenna element requires an RF feed cable with a power rating of greater than 200 W. As an initial estimate, we routed LMR-400 from each of the 8 antenna elements. The cable routing through the wing root in the upper cabin is visible in Figure 10 (red tubing). The final routing is subject to constraints from: 1) the aileron and flap control rods in the aft cabin, 2) fuel lines in the wing root, and 3) the ballistic parachute straps. The routing length from the outboard pylon #1 to the equipment rack is 5.5 m. This cable length corresponds to slightly less than 1 kg and 0.5 dB loss at 470 MHz with LMR-400.

The radar equipment weight is estimated at 40 kg. As this is less than a standard passenger, we use: 1) the existing seat rails mounted to the seat pan area, and 2) the seat belt attach points as the structural load paths. Interaction with the aircraft manufacturer is prudent for additional internal hardpoints. The seat pan is not flat, the equipment rack and attach structure will be specific to the aircraft.

3.3 Aircraft Performance

This design study evaluated the aircraft design specifications and feasibility in terms of performance, weight & balance (W&B), and equipment power. The nominal reference values for aircraft performance estimates are $S = 107.4 \text{ ft}^2$ and $CD_0 = 264$ counts. The aircraft performance with the full 8 element array installed is estimated as a 34 drag count increase (~ 12% increase in drag). At 75% cruise power, the flight range is expected to be approximately 88% of the nominal aircraft range. We expect that a drag cleanup study and potential antenna miniaturization will increase the aircraft range by 2 to 5%.

The internal radar systems (i.e. Tx/Rx, digital systems, a data server, and power systems connected into an equipment rack) must be integrated within the size, weight, and volume constraints of the CTLS aircraft. Additionally, these systems must remain clear of existing FCS, a pilot, and a semi-to-fully autonomous FCS in concurrent development

We created a weight & balance (W&B) estimate of the full integrated radar and aircraft system to reflect the radar and digital system design choices and experimentally determined system weights. The center of gravity (CG) of the fully integrated aircraft remains within the acceptable range of 11.1 inches to 18.8 inches aft of the leading edge.

The aircraft's primary electrical bus is a 12V system with an auxiliary 24V 1.5 kW alternator system feeding a dedicated equipment bus. Our initial power budget estimate is 800 W continuous with a 120VAC power input to the equipment rack UPS.

4 Experimental Results

4.1 Surface Operations in Greenland

The prototype transmitter and receiver and the digital system units were tested on the ice sheet of Greenland (EastGRIP) in July and August of 2019 to sound and measure ice layers to a bed depth of 2.7 km. The 8 element radar system was towed behind a surface vehicle.

4.2 Antenna Prototype

We built a prototype (Fig 11) of the antenna, balun, and pylon for RF, configuration, and structural evaluations. This prototype uses 1" and 7/8" aluminum tubing with 0.035 inch wall thicknesses. We used a 1 inch FR4 fiberglass reinforced composite pipe as the dipole connector



Fig 11. Prototype sleeved dipole antenna

sleeve, which provides both dipole structural bending stiffness and alignment. Screws connect the sleeve and tubes, which have flush-mounted nutplates installed into the inner wall. Polyethylene bowties connect the dipole elements and parasitic elements and provides a structural attach point to the pylon. Nose-cones cap the forward element tubes. As this prototype is designed for functional testing of the antenna and pylon system, the RF feed is constructed of connectorized RF components despite the weight penalty. We plan a switch to an integrated coax cable, balun, and feed in a future iteration. Our prototype of the antenna, pylon, and connectorized balun shown in Figure 11 weighs 0.94 lbs (492g). This is below the target weight.

We tested the prototype antenna and pylon with a Fieldfox vector network analyzer to characterize the RF performance. The test was performed outdoors and with a metallic ground plane to simulate the aircraft's wing (Fig

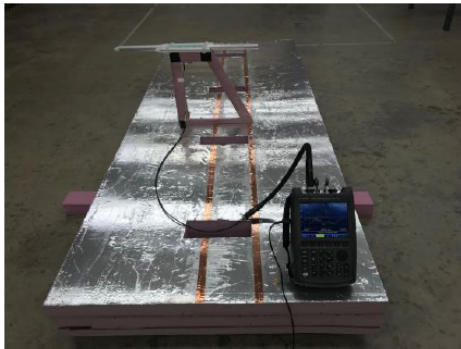


Fig 12. Field test configuration with antenna, simulated wing, and a portable VNA

12). The test was conducted between 100 to 500 MHz for

a single element. Figure 13 is representative of the performance as installed on the CTLS aircraft and provides

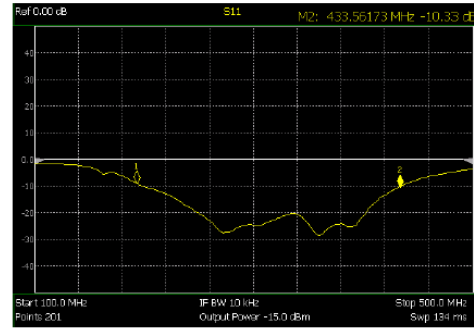


Fig 13. Simulated impulse response for ice bed returned signal

an experimentally measured -10dB bandwidth of 200 to 430 MHz. The measured return loss about 20 dB or lower over the frequency range of 240 to 400 MHz.

5 Conclusions

An 8 channel UWB radar system was developed for an LSA aerial platform for bed and ice-layer measurements in Polar regions. We have designed, constructed, and tested sub-systems including Polar testing in Greenland.

6 Acknowledgements

This project is supported by the Korean Polar Research Institute and the University of Alabama (UA). We wish to acknowledge the assistance of staff and students at the Remote Sensing Center at UA.

7 References

- [1] P. Fretwell, H. Pritchard, D. Vaughan, J. Bamber, N. Barrand, R. Bell and C. Bianchi, "Bedmap2: Improved Ice Bed, Surface and Thickness Datasets for Antarctica.," *Cryosphere.*, 2013.
- [2] R. Thomas, E. Frederick, J. Li, W. Krabil, S. Manizade, J. Paden, J. Sonntag, R. Swift and J. Yungel, "Accelerating Ice Loss from the Fastest Greenland and Antarctic Glaciers.," *Geophysical Research*, 2011.

Open-Sleeve Dipole Antenna for an Airborne VHF/UHF Snow Measuring Radar*

Hoyun Won, Yang-Ki Hong, Briana Bryant, Linfeng Li, Minyeong Choi, Charles O'Neill, Jie-Bang Yan, and Prasad Gogineni

Department of Electrical and Computer Engineering and Remote Sensing Center
The University of Alabama, Tuscaloosa, AL 35487, USA

hwon@crimson.ua.edu, ykhong@eng.ua.edu, bmbryant1@crimson.ua.edu, lli78@crimson.ua.edu, mchoi11@crimson.ua.edu, croneill@eng.ua.edu, jbyan@ua.edu, pgogineni@ua.edu

Abstract—A simple, ultrawideband, and high gain VHF/UHF open-sleeve dipole antenna and array for airborne snow measuring radar are presented. To satisfy the desired bandwidth of 300 MHz and realized gain of 10 dBi or higher in the frequency range of 170 and 470 MHz, the geometry and dimensions of the antenna are optimized using various parametric studies under the real aircraft wing structure. The simulation results show that the 4-element antenna array having a dipole length of 720 mm, a parasitic element length of 280 mm, a separation between dipole and a parasitic element of 64 mm, and separation between antenna elements of 640 mm satisfies the desired bandwidth and gain requirements.

Keywords—Airborne radar, VHF/UHF array, open-sleeve dipole

I. INTRODUCTION

Due to rapid sea-level rise from polar ice sheets melting, measuring ice sheet thickness, and imaging the ice-bed interface of the polar ice sheets have become essential tasks to accomplish [1]. One of the established methods to accomplish the tasks is to use airborne VHF/UHF radar due to constant attenuation of the radio signals in the VHF/UHF frequency range during their penetrating through the ice sheets. Thus, many VHF/UHF antennas were developed to image the ice-bed interface [1-2]. F. Rodriguez-Morales *et al.* [1] developed a folded dipole antenna, which operates at the center frequency of 195 MHz to measure the ice thickness. Although the structure of the antenna is simple, the antenna suffers from a narrow bandwidth (B) of 60 MHz. J. Yan *et al.* [2] reported a polarization-reconfigurable low-profile ultrawideband planar dipole antenna that operates from 150 to 550 MHz (B of 400 MHz). Still, it requires a complicated antenna enclosure and a large size. Likewise, other reported VHF/UHF antennas suffer from either or both the above issues [1-2].

In this paper, we develop a simple, ultra-wideband, and high gain open-sleeve dipole antenna and 4-element antenna array for an airborne VHF/UHF radar. The antenna realizes the B of 300 MHz with only three hollow aluminum tubes. We simulate the antenna and array performance under the real wing structure of the Flight Design CTLS aircraft, using ANSYS High-Frequency Structure Simulator (HFSS 2019 R2); therefore, the simulated antenna performance is more realistic.

II. ANTENNA DESIGN AND SIMULATION

Fig. 1 shows the geometry and dimension of the open-sleeve dipole antenna under the Flight Design CTLS aircraft left wing.

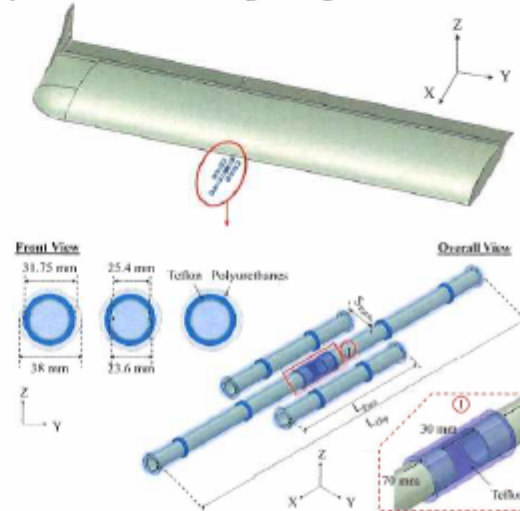


Fig. 1. Overall view of the sleeve dipole antenna under carbon fiber reinforced epoxy composites-based wing with specifications

The antenna consists of a dipole antenna, which is fed by 100Ω coaxial cable, and parasitic element on each side of the dipole. To reduce the weight of the antenna and maintain high strength, a commercial 2024 aluminum tube, having the outer diameter of 25.4 mm and the wall thickness of 0.89 mm, is used for both dipole and parasitic elements. Further, the polyurethane fiberglass frame (relative permittivity (ϵ_r) of 1.08 and dielectric loss tangent ($\tan\delta_e$) of 0.0016) is used to cover the antenna to resist aerodynamic pressure and allow RF cable and balun insertion [3]. To rigidly hold the separated dipole and antenna within the polyurethane fiberglass frame, a Teflon tube (ϵ_r of 2.1 and $\tan\delta_e$ of 0.001) is used [4]. Lastly, the realistic CTLS wing model (1300 mm wide, 3700 mm long, and 150 mm thick) with carbon fiber reinforced epoxy composite, having an electrical conductivity of 19,000 siemens/m, is used in simulation [5]. The antenna is placed 420 mm under the wing.

*Supported in part by Korea Polar Research Institute

III. RESULTS AND DISCUSSION

This funded project needs the antenna to operate between 170 and 470 MHz (B of 300 MHz) with a realized gain at boresight (RG) of 10 dBi or higher. To obtain the necessary B and RG, we have performed a parametric study of the dipole length (L_{Dip}), parasitic length (L_{Para}), and separation between

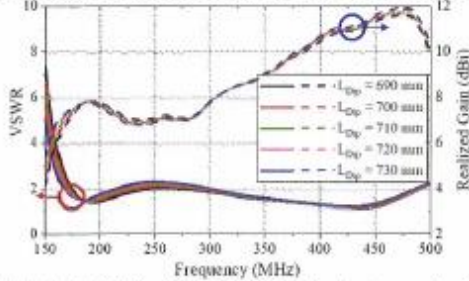


Fig. 2. Simulated VSWR and RG of the sleeve dipole antenna with different lengths of a dipole element (L_{Dip}).

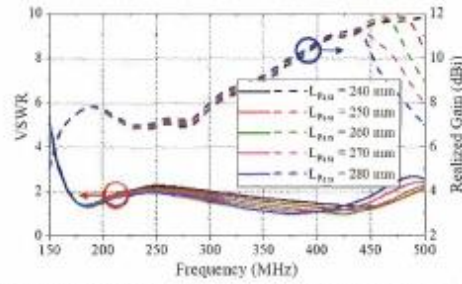


Fig. 3. Simulated VSWR and RG of the sleeve dipole antenna with different lengths of a parasitic element (L_{Para}).

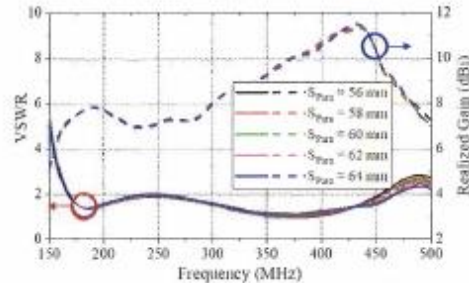


Fig. 4. Simulated VSWR and RG of the sleeve dipole antenna with different separations of a parasitic element (S_{Para}).

dipole and parasitic elements (S_{Para}). In this antenna performance simulation, the voltage standing wave ratio (VSWR) below 2 is considered as the bandwidth of the antenna.

Firstly, we conducted the parametric study of L_{Dip} to set the first crossing frequencies of the VSWR below 2 (f_{first}) to 170 MHz. Fig. 2 shows the simulated VSWR and RG with different L_{Dip} when L_{Para} and S_{Para} are 250 and 58 mm, respectively. Among different L_{Dip} , the antenna with an L_{Dip} of 720 mm achieves the f_{first} of 170 MHz and high last crossing frequencies of the VSWR below 2 (f_{last}) of 489 MHz.

Although both f_{first} and f_{last} were satisfied, the antenna with an L_{Dip} of 720 mm showed the VSWR above 2 between 216 and

304 MHz. Thus, to reduce the VSWR across these frequency ranges, the parametric study of L_{Para} was performed. Fig. 3 shows the simulated VSWR and RG of different L_{Para} for L_{Dip} of 720 mm and S_{Para} of 58 mm. The antenna with L_{Para} of 280 mm showed the VSWR below 2 in the frequency of interest. However, the f_{last} decreased to 455 MHz from 489 MHz.

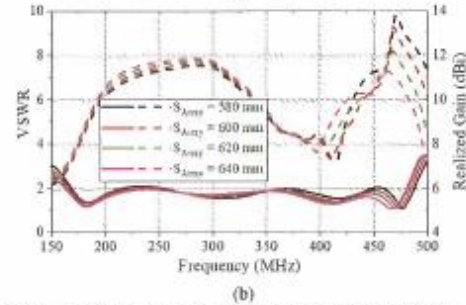
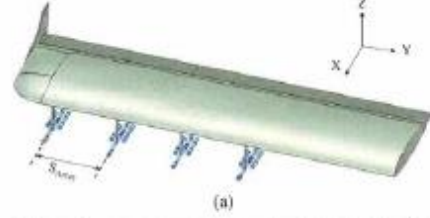


Fig. 5. (a) Overall view and (b) simulated VSWR and RG of the sleeve dipole antenna array with different separations of an array element (S_{Array}).

Thus, to increase the f_{last} , different S_{Para} was investigated when the L_{Dip} and L_{Para} are 720 and 280 mm, respectively. The results in Fig. 4 confirm that the antenna with S_{Para} of 64 mm meets the f_{last} of 470 MHz.

Lastly, to increase the RG up to 10 dBi, a 4-element antenna array, separated by the length of S_{Array} , is adopted, as shown in Fig. 5(a). As Fig. 5(b) shows, the S_{Array} of 640 mm exhibits the RG above 10 dBi for 200 MHz, which is 15-22 MHz higher frequencies than other S_{Array} , while satisfying the VSWR requirements. In summary, the antenna array, which has an L_{Dip} of 720 mm, L_{Para} of 280 mm, S_{Para} of 64 mm, and S_{Array} of 640 mm can be applied to an airborne VHF/UHF radar.

IV. CONCLUSION

An ultrawideband and high gain VHF/UHF open-sleeve dipole antenna and array are developed and optimized for airborne snow measuring radar. The optimized array realized the bandwidth requirement of 300 MHz (170-470 MHz) and realized the gain requirement of 10 dBi or higher for 200 MHz.

REFERENCES

- [1] F. Rodriguez-Morales, et al., "Advanced Multifrequency Radar Instrumentation for Polar Research," IEEE Trans. Geosci. Remote Sens., 52 (5) pp. 2824, May. 2014.
- [2] J. Yan, et al., "A Polarization Reconfigurable Low-Profile Ultrawideband VHF/UHF Airborne Array for Fine-Resolution Sounding of Polar Ice Sheets," IEEE Trans. Antennas Propag., 63 (10), pp. 4334, Oct. 2015.
- [3] G. Meyer, "Polyurethane Foam: Dielectric Materials for Use in Radomes and other Applications," General Plastics Manufacturing Company, November 3, 2015.

[4] F. Sears, M. Zemansky, and H. Young, *University Physics*, 6th ed, Addison-Wesley, 1982. [Online] <http://hyperphysics.phy-astr.gsu.edu/hbase/Tables/diel.html>

[5] M. Leininger, F. Thurecht, E. Pfeiffer, and A. Ruddle, "Advanced Grounding Methods in the Presence of Carbon Fibre Reinforced Plastic Structures," Proc. 2012 ESA Workshop on Aerospace EMC, May 2012.

Warning

- 1. This report is a report of research results of a project entrusted by the Korea Polar Research Institute.**
- 2. When you present the contents of this report, you must state that these contents are research results of a project entrusted by the Korea Polar Research Institute.**
- 3. Materials concerning the nation's classified science and technology information must not be presented or disclosed.**